Development of a Composite Material Aerodynamic Demise Model for the Object Reentry Survival Analysis Tool (ORSAT)

Priscilla A. Mendoza [(1)], Benton R. Greene [(2)], and Chris L. Ostrom [(3)]

[(1)] The University of Texas at El Paso, 500 W University Avenue, El Paso, TX, 79968; pamendoza4@miners.utep.edu
[(2)] Jacobs, NASA Orbital Debris Program Office, NASA Johnson Space Center, Mail Code XI5-B9E, 2101 NASA Parkway, Houston, TX 77058, USA, benton.r.greene@nasa.gov
[(3)] NASA Orbital Debris Program Office, NASA Johnson Space Center, Mail Code XI5-B9E, 2101 NASA Parkway Houston, TX 77058, USA, christopher.l.ostrom@nasa.gov

Abstract

The reentry demise of fiber-reinforced polymer (FRP) composites is an increasing concern for modern spacecraft at end of life. Unlike traditional materials such as metals, shredding of the material by aerodynamic forces appears to be a major component of the reentry demise mechanism. This paper will describe a new mechanical, strength-based, material demise model for the Object Reentry Survival Analysis Tool (ORSAT) Version 7.1. The model is based on laboratory in-situ and residual strength tests of several FRP materials performed during the NASA Orbital Debris Program Office's Phase II Composite Material Demise test campaign.

To test the residual strength of partially charred FRP materials, the authors tested 107 rectangular shaped samples of different thicknesses that were previously exposed to high-enthalpy flow at the University of Texas at Austin's Inductively Coupled Plasma Torch facility. Tests were performed under normal atmospheric conditions at NASA Johnson Space Center's Experimental Impact Laboratory using a Chatillon TCD1000 tensile test machine configured with a three-point bending jig. Mean fracture load, residual strength, delamination, and flexural modulus were measured for each test. An engineering model of aeromechanical demise for each material was developed by correlating the measured residual strength of the samples with the duration and magnitude of the applied heat flux and the mass loss and char progression. This model has been implemented in ORSAT 7.1 for the built-in, charring carbon fiber/epoxy and charring glass fiber/epoxy material models.

The new model was verified by calculating the demise of hundreds of FRP composite fragments of various shapes and sizes and checking the calculations for consistency, with specific focus on material characterization in one-dimension. Further tests are planned in hypersonic flow facilities to validate the assumptions used in the model.

1 Introduction

Estimating the risk of human casualty from uncontrolled reentry of space debris is an increasingly important task as more satellites are launched and operators are opting for natural decay and reentry as the disposal option of choice. Many modern spacecraft include large structural components made of fiber reinforced polymer (FRP) materials like carbon fiber and fiberglass. This presents a problem for casualty risk estimation as the exact behavior of FRPs during reentry is still not well understood despite many advances in this field in recent years [1] [2] [3] [4].

One-dimensional heat transfer through a charring graphite epoxy composite was investigated as far back as 1980 using a continuous wave CO_2 laser energy source to produce surface heat fluxes of up to 2.79 kW/cm^2 [5]. The behavior of composites in a fire environment, which is analogous though with a

much lower typical heat flux is summarized by [6] and [7]. Some work on strength of carbon fiber materials in fire has also been done [8], and has proven relevant to the current work.

This paper details some of the advances in calculating the demise of FRP satellite components incorporated in the latest version of ORSAT, version 7.1, that have come out of the laboratory testing conducted by the NASA Orbital Debris Program Office (ODPO) as part of an ongoing composite material demisability test campaign.

1.1 ICP Torch Facility

The University of Texas (UT) Wind Tunnel Lab's Inductively Coupled Plasma (ICP) Torch facility consists of a 50 kW inductively coupled plasma generator, pictured in Fig. 1. The facility operates at room pressure and provides easy access for changing test samples and instrument probes. Room pressure operation also allows for excellent optical access for many remote measurements like optical pyrometers and video cameras. The torch itself can generate plasma streams of argon or air plasma at flow rates up to 80 standard liters per minute and temperatures up to 7000 K for air and 10,000 K for argon [9]. The diameter of the plasma plume is 30 mm.

The facility provides two water-cooled motorized sting arms, also shown in Fig. 1, for mounting test samples and instrument probes. The water-cooling allows the probe or sample to be inserted into the plasma stream for an indefinite period.

Fig. 1. Photograph of ICP torch in operation.

1.2 Composite Demisability Test Campaign

The ODPO's composite demisability test campaign, beginning in 2017 and continuing with further tests in 2019, collected data on all aspects of the thermal demisability of FRP materials: pyrolysis rates, *in-situ* strength at pyrolysis temperatures, and residual strength after pyrolysis. Data from this campaign on pyrolysis rate and *in-situ* strength have been discussed in previous work [10] [11], and were incorporated into the pyrolysis model for FRPs in ORSAT 7.0.

In addition to understanding the pyrolysis of the materials, it is important to understand how the degradation from pyrolysis affects the ability of the shear and compressive forces of the atmosphere to

break the material into small, harmless chaff. Since the peak dynamic pressure often occurs after the peak heat pulse in a typical LEO reentry, the relevant property of the material is the residual strength after the material has significantly cooled.

2 Test Design

Residual strength of the FRP materials investigated was determined by exposing test samples to the plasma for a set amount of time and testing the bending strength afterward in a tension test machine. The data was then compiled for multiple exposure times to show how the material responded to different durations and intensities of heat pulse.

2.1 Sample Coupons

To minimize complexity, all test samples were cut to the same planform-size rectangular coupon. The rectangular coupon shape allowed a 4-point bending load to be easily applied to the sample during exposure to the plasma using a simple set of counterweighted jaws. These jaws could then be used to hold all samples not placed under load by simply offsetting the lower jaws from the upper. Fig. 2 shows a diagram of the test sample holder.

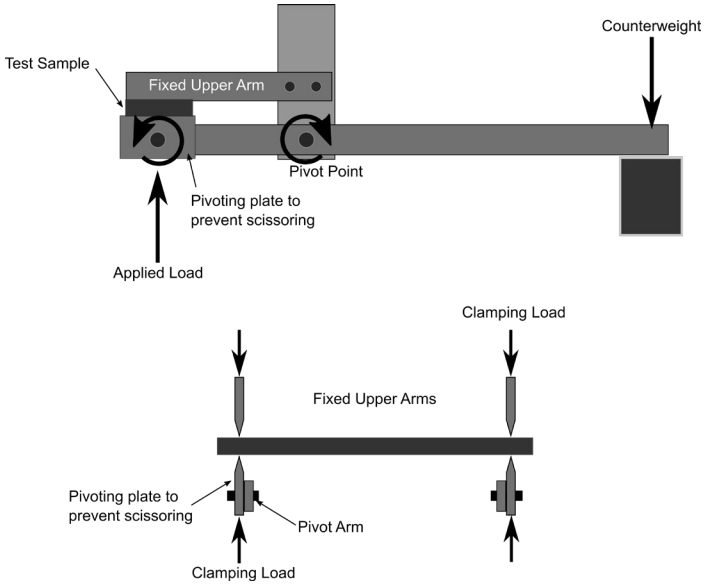

Fig. 2. Diagram of clamping mechanism for holding test samples in plasma torch.

Rectangular coupons 1 to 3 mm thick were used for the residual strength static loading tests. All the coupons were 80 ± 0.7 mm long by 25 ± 0.2 mm wide. The exact thickness of the coupon depended on the available stock of the given material.

The materials used were chosen to be representative of common materials used in spacecraft construction. Carbon fiber-reinforced polymer (CFRP) made using epoxy resin, vinyl ester resin, and cyanate ester resin and glass fiber-reinforced polymer (GFRP) made using epoxy resin were all tested. Commercial off-the-shelf (COTS) panels of epoxy resin CFRP and G10 (a specific epoxy resin GFRP used in printed circuit boards) were also included in the test samples. In addition, in-house layups of epoxy CFRP, vinyl ester CFRP, and cyanate ester CFRP were included to evaluate a full variety of polymers that would be exposed during the spacecraft reentry process. Table 1 lists the materials and number of coupons tested for each.

Table 1. List of Sample Coupon Materials and Quantities

Material	Quantity
COTS Epoxy CFRP	24
COTS Epoxy GFRP	24
Hand layup Epoxy CFRP	24
Hand Layup Vinyl Ester CFRP	24
Hand Layup Cyanate Ester CFRP	8
Total	**104**

2.2 Torch Conditions

Each material was exposed to nominal heat flux values of 20 W/cm² and 30 W/cm². Additionally, the effects of high-altitude levels of oxygen were simulated by mixing 2% oxygen into a pure argon test gas. Pure argon with no added oxygen was used as a control. Originally, the test plan called for heat flux values of 30 W/cm² and 50 W/cm², but after difficulty achieving the higher value using the pure argon test gas, the lower value of 20 W/cm² was used. To measure the change in residual material strength over time, test samples were inserted over four different durations at each plasma condition: 5, 10, and 15. Table 2 summarizes the test conditions, exposure durations and the number of test samples exposed to each. To have redundancy while maximizing the number of different conditions tested in the limited facility time available, two samples were tested at each condition.

Table 2. Test condition matrix showing number of tests at each condition

Air %	*Heat Flux (W/cm²)*	*Exposure Time (s)*		
		5	**10**	**15**
0	20	2	2	2
2	20	2	2	2
0	30	2	2	2
2	30	2	2	2

2.3 Bending Test

After exposure to the plasma, the samples were placed in a bending test rig on the tensile test machine. A 4-point bend test was originally planned using the same geometry as the *in-situ* bending test, also used in the test campaign. After testing a few samples with this configuration, it became clear that the bending rig jaws interfered with the sample before complete sample failure. Using a 3-point bending configuration mitigated this problem and the remaining tests were performed using a 3-point bending load. Both configurations are pictured in Fig. 3.

Bend tests were performed by applying a constant strain rate of 0.4 in/min (0.1693 mm/s) until inelastic failure of the sample was observed or the jaws reached their maximum displacement. The load versus displacement curve was recorded for the test, and the maximum load at failure was taken to be the ultimate load. The ultimate load, test sample dimensions, and the maximum 3-point bending stress equation in Eq. 1 were used to calculate the ultimate bending stress, σ_{ult}, of each coupon, where P_{ult} is the ultimate load, l is the distance between the support points, w is the width of the sample, and t is the sample thickness. For those tests performed before switching to the 3-point test configuration, the 4-point bending stress, Eq. 2, was used.

$$\sigma_{ult} = \frac{3P_{ult}l}{2wt^2} \quad (1)$$

$$\sigma_{ult} = \frac{6P_{ult}d}{wt^2} \quad (2)$$

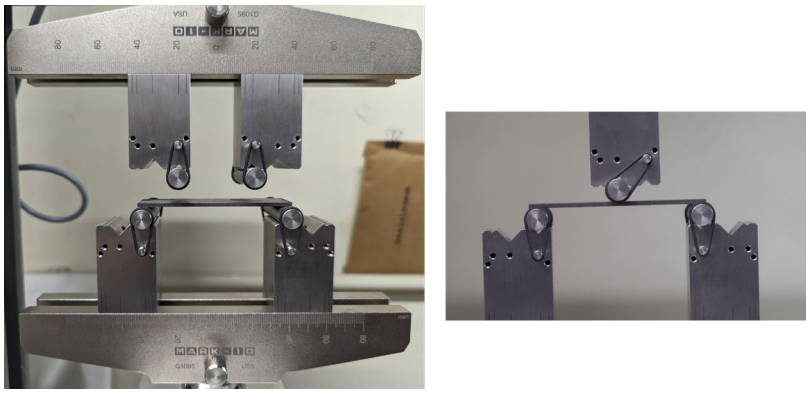

Fig. 3. Photograph of bending test rig in the original 4-point bend configuration (left), and the 3-point bend configuration (right).

3 Results

For most of the test samples, a failure point was reached that corresponded to a peak load. Many of the thinner samples proved too elastic to fail within the vertical travel limits of the testing apparatus, even with the increased vertical travel allowed by the 3-point bend configuration. For these, the load at maximum displacement was recorded.

It was also found that some of the samples exposed to the plasma for the longest period had so little rigidity left that the bending load barely registered on the most sensitive available load cell. These samples similarly failed to “fail” in the strictest sense.

3.1 Load/Displacement Curves

An automated script analyzed the load/displacement curves for each sample to locate the elastic region, point of maximum load, and ultimate load. Most of the samples displayed the characteristic behavior shown in Fig. 4, with a clear linear region and an inflection point at structural failure. Most samples also displayed the nonlinearity evident in the first millimeter or so of the displacement in Fig. 4. This is due to a slight twist in the sample that flattens out in the first 1 to 2 mm of travel after the load point makes contact. The increase in load at the end of travel is due to the sample contacting a different part of the load jig. This also happened on many samples but is easily ignored.

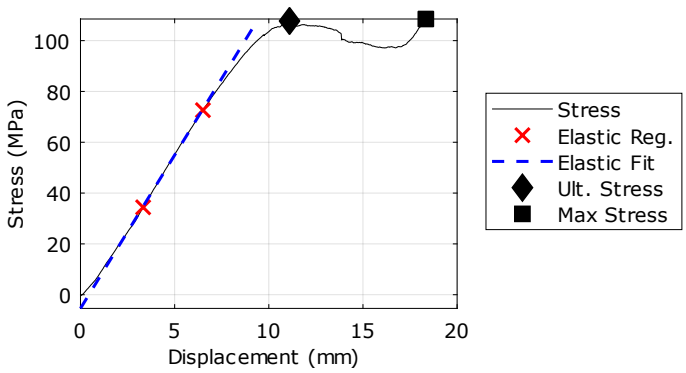

Fig. 4. Typical stress/displacement curve measured in 3-point bending tests.

The stress curve in Fig. 5 shows how a very low-rigidity sample still displays the classic stress-strain curve. The elastic region, while much smaller, is still very distinct and there is a clear inflection at the ultimate failure point.

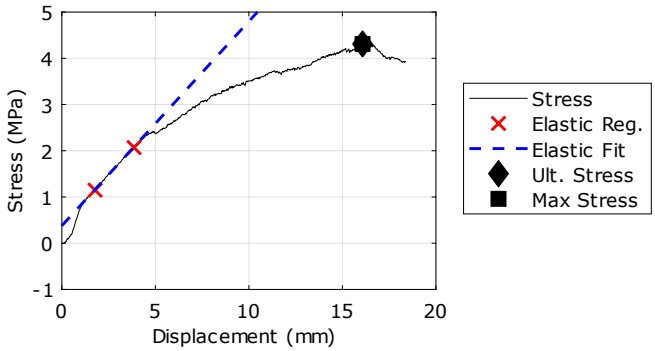

Fig. 5. Typical stress/displacement curve for low-rigidity samples.

A final observation was that some samples experienced multiple, distinct step failures. This is best illustrated by Fig. 6. After the initial failure at 4.5 mm of displacement, the load increases for a brief period before a second failure at 7 mm of displacement and increases slightly before a third failure at 10 mm of displacement. Like in Fig. 4, the final increase in load at 15 mm of displacement is due to contact of the sample with another part of the loading apparatus and is not representative of the 3-point bending failure.

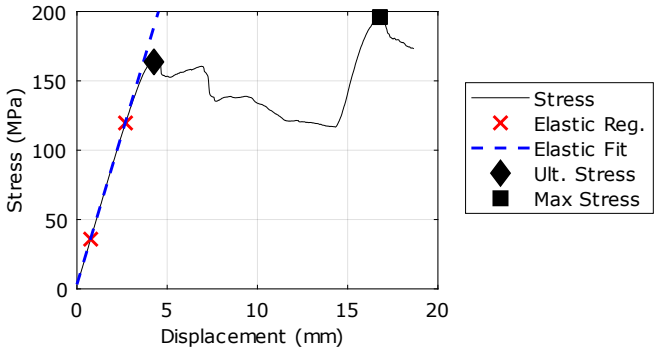

Fig. 6. Load curve of sample showing multiple step failures.

3.2 Ultimate Stress

After analyzing the load curves, an ultimate stress was found for 88 of the 104 sample coupons. These are shown in Fig. 7 for the carbon fiber epoxy and fiberglass materials and Fig. 8 for the cyanate and vinyl ester carbon fiber materials.

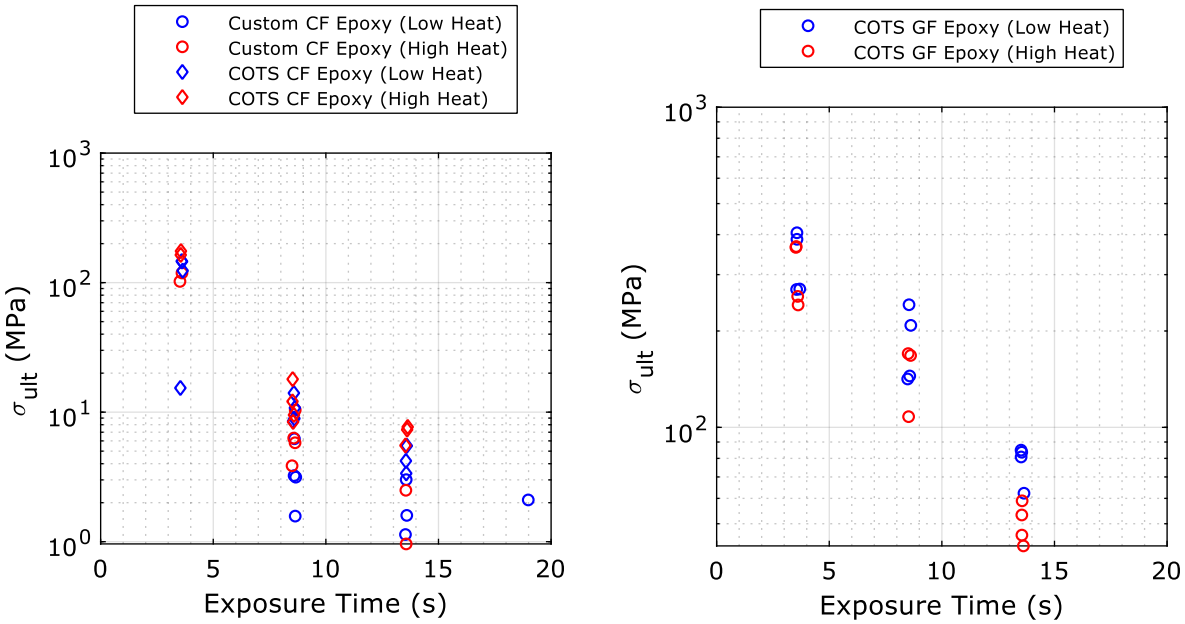

Fig. 7. Plot of ultimate strength of COTS and custom CF epoxy (left) and COTS GF epoxy (right) for low and high heat flux at each exposure duration.

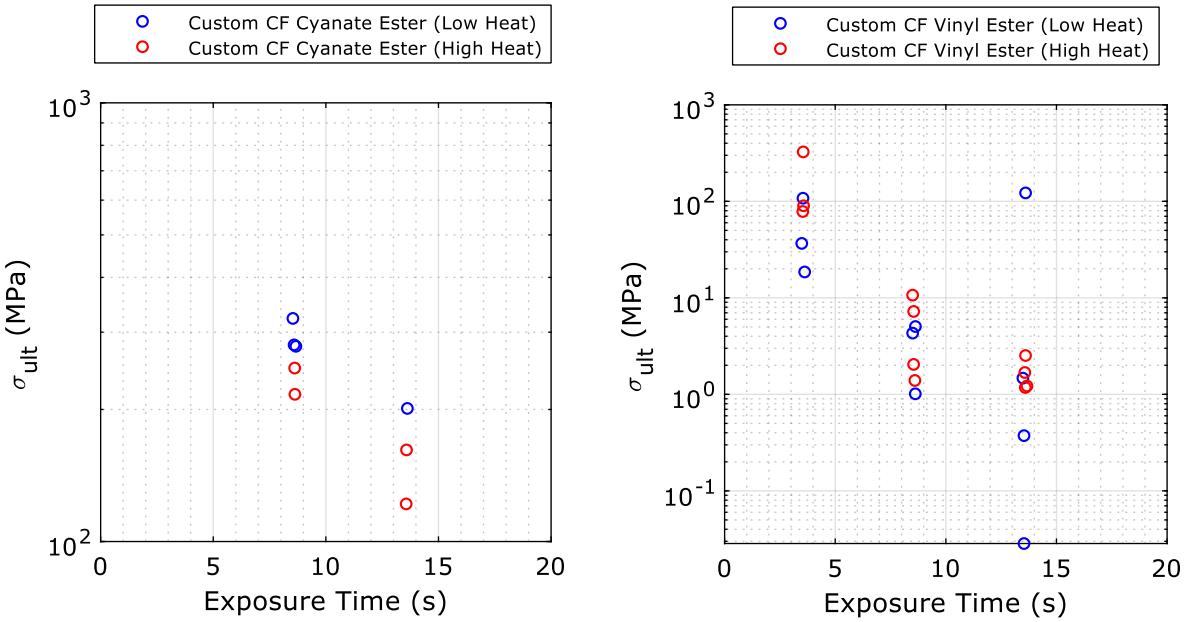

Fig. 8. Plot of ultimate strength of custom CF cyanate ester (left) and COTS CF vinyl ester (right) for low and high heat flux at each exposure duration.

The ultimate strength for the fiberglass and cyanate ester materials behaved as expected, with the high heat flux reducing the strength faster than the cold heat flux, and the strength decreasing logarithmically with exposure time. The epoxy and vinyl ester resins appear to display the opposite trend with heat flux, though this may be due to scatter in the data and a relatively weak dependence on heat flux for the range of values tested.

4 Strength Model

Creating a model of the ultimate stress of FRP materials useful for ORSAT requires condensing the data into a correlation between one or two variables that ORSAT can calculate and the ultimate strength of the material in that state. Considering residual strength once all coupons have returned to room temperature, only three measurable quantities are different between the various coupons of a given material: char thickness, overall thickness, and mass loss. One of the core assumptions of the thermal transport model that ORSAT uses is that the overall size of an object does not change, so a change in overall thickness due to aeroheating and pyrolysis is not a value that ORSAT can calculate.

This leaves char thickness and mass loss. These are already calculated by the pyrolysis model implemented in ORSAT 7.0. The mass loss is calculated for the sample coupons by subtracting the measured final mass from the measured initial mass. To make the value as general as possible, it is best to normalize by the initial mass to find mass loss fraction. Unfortunately, the char thickness is not as easily measured in the tested coupons, but it can be estimated by using the average charring rate from the pyrolysis model and the known exposure time.

To determine which of these variables to use in the strength model, the data are fit to an exponential function and the R^2 and root mean square error for the fits are compared. A pyrolysis model is only available for carbon fiber epoxy and glass fiber epoxy, so these are used for the comparison. The R^2 values of the fits for each material are given in Fig. 9. As a check, the R^2 value for the correlation between mass loss fraction and char penetration fraction is also shown for each material.

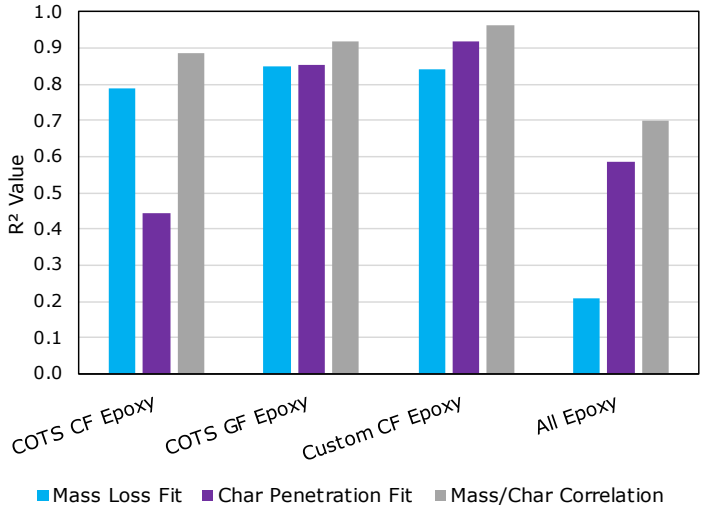

Fig. 9. Comparison of goodness of fit for mass loss and char penetration, and the correlation between mass loss and char penetration.

For the GFRP samples and the thin hand-layup CF epoxy samples, the choice of char penetration or mass loss does not make much difference; however, the COTS CFRP and the combination of all CF epoxy samples show major differences in the quality of the fit between the two variables.

A comparison of the fits for all carbon fiber epoxy sample coupons, both custom layup and COTS, is shown in Fig. 10 and illustrates how seemingly two distinct clusters in stress versus mass loss get blended together in stress versus char penetration. This is because the char penetration is the peak value, and the actual char front in the sample coupon is 3D and non-uniform in both length and width directions. Therefore, for a thicker coupon, the mass loss for the same peak char penetration will be lower. The much worse correlation between mass loss and char penetration for all CF epoxy in Fig. 9 corroborates this interpretation.

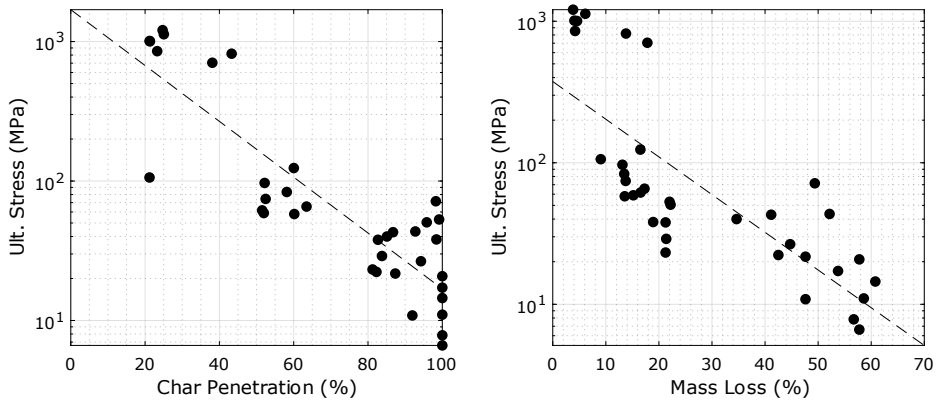

Fig. 10. Comparison of the fit for ultimate stress versus char penetration (left) and for ultimate stress versus mass loss (right) for all carbon fiber epoxy samples.

Since all sample coupons for the GFRP material were the same thickness, this disparity does not appear in those fits, but it does indicate that char penetration is the appropriate variable for predicting the degradation of the material strength.

5 ORSAT Implementation

ORSAT 7.1 introduces a new subroutine for calculating the ultimate stress of a pyrolyzing material that accepts the char depth as an input and uses the correlations derived in the previous section to calculate the approximate ultimate stress of the material at that time step. For custom pyrolyzing materials, a feature has been added to the input file that allows the user to input custom fit coefficients or a lookup table of char penetration and ultimate stress.

At each time step, the ultimate stress is compared to the maximum bending stress in the fragment, calculated from the dimensions of the fragment and the dynamic pressure using an analytic equation derived for each shape primitive supported by ORSAT. The key assumptions for the derivation of the analytic equations for stress are:

- The primary load on the structure of the fragment is a crushing load from the drag force acting against the inertia of the object
- Maximum stress occurs at the maximum bending moment
- Shear stress can be ignored
- Each material layer contributes to the tensile and compressive stress counteracting the bending moment

6 Future Work

An engineering model for ultimate stress and aerodynamic demise of pyrolyzing FRP materials was developed and implemented in ORSAT 7.1 using laboratory test data for residual strength in charred FRP materials. Full testing and verification of the ORSAT implementation of the ultimate stress subroutine remains to be performed. Additionally, there are plans to validate some of the assumptions used in deriving the model with a series of hypersonic wind tunnel tests.

7 References

1. Fritsche, B. (April 22-25, 2013). Modeling the Thermal Decomposition of Carbon Fibre Materials During Re-entry. In 6th European Conference on Space Debris, Darmstadt, Germany.
2. Pontijas Fuentes, I., *et al.* (2019). Upgrade of ESA's Debris Risk Assessment and Mitigation Analysis (DRAMA) tool: Spacecraft Entry Survival Analysis Module. Acta Astronautica. **158**, pp148-160.
3. Greene, B.R. (2020). "Composite Material Char Rate and Strength Retention Study at University of Texas Austin," Orbital Debris Quarterly News. **23**(2), pp5-6.
4. Greene, B.R., Ostrom, C.L., & Marichalar, J. (2022). "Updates to Thermal Demise Model in Object Reentry Survival Analysis Tool, Version 7.0," Orbital Debris Quarterly News. **26**(3), pp8-10.
5. Griffis, C.A., Masumura, R.A., & Chang, C.I..(1981). Thermal Response of Graphite Epoxy Composite Subjected to Rapid Heating. US Naval Research Laboratory, Washington, D. C..
6. Blasi, C.D. (2000). The State of the Art of Transport Models for Charring Solid Degradation. Polymer International. **49**(10), pp1133-1146.
7. Gibson, A.G., Feih, S., & Mouritz, A. (2011). Developments in Characterising the Structural Behaviour of Composites in Fire. In Composite Materials: A Vision for the Future, (Eds. L. Nicolais, E. Milella & M. Meo) London, U.K., Springer, pp187-217.
8. Burns, L.A., Feih, S., & Mouritz, A. (2009). Fire-Under-Load Testing of Carbon Epoxy Composites. In 47th Aerospace Sciences Meeting, Orlando, FL.
9. Greene, B.R., *et al.* (2017). Characterization of a 50 kW Inductively Coupled Plasma Torch for Testing of Ablative Thermal Protection Materials. In AIAA SciTech Forum - 55th AIAA Aerospace Sciences Meeting, Grapevine, TX.
10. Greene, B.R., & Sanchez, C.M. (May 15-17, 2019). Demisability of GFRP and CFRP Components of Reentering Orbital Debris: Phase I Test Results. In 10th International Association for the Advancement of Space Safety Conference, El Segundo, CA.
11. Greene, B.R., & Ostrom, C.L. (2021). Pyrolysis Rate and Yield Strength Reduction in Carbon Fiber and Glass Fiber Composites Under Reentry Heating Conditions. In 8th European Conference on Space Debris, Darmstadt, Germany.